remote sensing

MDPI

Article

Correlation Analysis of Vertical Ground Movement and Climate Using Sentinel-1 InSAR

Francesco Pirotti [1,2,*], Felix Enyimah Toffah [1,3] and Alberto Guarnieri [1,2]

[1] Interdepartmental Research Center of Geomatics (CIRGEO), University of Padova, Viale dell'Università 16, 35020 Legnaro, Italy; felixenyimah.toffah@uniroma1.it (F.E.T.); alberto.guarnieri@unipd.it (A.G.)
[2] Department of Land, Environment and Agro-Forestry (TESAF), University of Padova, Viale dell'Università 16, 35020 Legnaro, Italy
[3] Department of Civil, Building and Environmental Engineering, Sapienza University of Rome, Via Eudossiana 18, 00184 Rome, Italy
* Correspondence: francesco.pirotti@unipd.it

Abstract: Seasonal vertical ground movement (SVGM), which refers to the periodic vertical displacement of the Earth's surface, has significant implications for infrastructure stability, agricultural productivity, and environmental sustainability. Understanding how SVGM correlates with climatic conditions—such as temperatures and drought—is essential in managing risks posed by land subsidence or uplift, particularly in regions prone to extreme weather events and climate variability. The correlation of periodic SVGM with climatic data from Earth observation was investigated in this work. The European Ground Motion Service (EGMS) vertical ground movement measurements, provided from 2018 to 2022, were compared with temperature and precipitation data from MODIS and CHIRP datasets, respectively. Measurement points (MP) from the EGMS over Italy provided a value for ground vertical movement approximately every 6 days. The precipitation and temperature datasets were processed to provide drought code (DC) maps calculated ad hoc for this study at a 1 km spatial resolution and daily temporal resolution. Seasonal patterns were analyzed to assess correlations with Spearman's rank correlation coefficient (ρ) between this measure and the DCs from the Copernicus Emergency Management Service (DC_{CEMS}), from MODIS + CHIRP (DC_{1km}) and from the temperature. The results over the considered area (Italy) showed that 0.46% of all MPs (32,826 MPs out of 7,193,676 MPs) had a ρ greater than 0.7; 12,142 of these had a positive correlation, and 20,684 had a negative correlation. DC_{1km} was the climatic factor that provided the highest number of correlated MPs, roughly giving +59% more correlated MPs than DC_{CEMS} and +300% than the temperature data. If a ρ greater than 0.8 was considered, the number of MPs dropped by a factor of 10: from 12,142 to 1275 for positive correlations and from 20,684 to 2594 for negative correlations between the DC_{1km} values and SVGM measurements. Correlations that lagged in time resulted in most of the correlated MPs being within a window of ±6 days (a single satellite overpass time). Because the DC and temperature are strongly co-linear, further analysis to assess which was superior in explaining the seasonality of the MPs was carried out, resulting in DC_{1km} significantly explaining more variance in the SVGM than the temperature for the inversely correlated points rather than the directly correlated points. The spatial distribution of the correlated MPs showed that they were unevenly distributed in clusters across the Italian territory. This work will lead to further investigation both at a local scale and at a pan-European scale. An interactive WebGIS application that is open to the public is available for data consultation. This article is a revised and expanded version of a paper entitled "Detection and correlation analysis of seasonal vertical ground movement measured from SAR and drought condition" which was accepted and presented at the ISPRS Mid-Term Symposium, Belem, Brasil, 8–12 November 2024. Data are shared in a public repository for the replication of the method.

Keywords: subsidence; drought; seasonal vertical ground movement; SAR; Sentinel-1; interferometric synthetic aperture radar (InSAR)

Citation: Pirotti, F.; Toffah, F.E.; Guarnieri, A. Correlation Analysis of Vertical Ground Movement and Climate Using Sentinel-1 InSAR. *Remote Sens.* **2024**, *16*, 4123. https://doi.org/10.3390/rs16224123

Academic Editors: Kristy Tiampo, Sergey Samsonov, Wanpeng Feng, Valentin O. Mikhailov and Guifang Zhang

Received: 15 September 2024
Revised: 27 October 2024
Accepted: 31 October 2024
Published: 5 November 2024

1. Introduction

Seasonal vertical ground movement (SVGM) refers to the vertical displacement of the ground surface, which follows harmonic trends, recurring every year and primarily driven by the changing seasons [1]. This displacement can manifest as either uplift (upward movement) or subsidence (downward movement), resulting in changes in surface elevation and posing significant threats to infrastructure, agriculture and environmental sustainability [2], and even playing a role in inundation scenarios from sea level rise [3]. SVGM is also a proxy for other phenomena that cause the deformation of the Earth's surface, such as earthquakes and tectonic activity [4], subsidence due to the extraction of groundwater [5] and volcanic activity [6]. Various factors drive SVGM, many of which are related directly or indirectly to the climate, e.g., the temperature and precipitation. Natural factors such as the compaction of sediment, geological processes and anthropogenic factors such as groundwater withdrawal are major contributors.

The temperature plays a significant role in SVGM. Directly, temperature fluctuations cause the thermal deformation of infrastructure—like buildings and roads—which can lead to the deformation of the infrastructure on the Earth's surface. Indirectly, the temperature affects the moisture content in soils and sediments, affecting their compaction and expansion. For instance, prolonged periods of high temperatures with little or no precipitation can lead to drought conditions, causing the ground to dry out and compact and result in subsidence. Conversely, in cooler, wetter seasons, soils absorb moisture, swell and exhibit uplift. This process can be understood through the principle of effective stress [7]: as the soil moisture increases, the pore water pressure rises, reducing the effective stress and causing uplift. In contrast, during droughts, reduced soil moisture decreases the pore water pressure, increasing the effective stress and leading to subsidence [8,9]. Thus, investigating the relations between these variables (temperature and drought) and SVGM will be crucial for proactive risk management and mitigation strategies.

SAR, defined as synthetic aperture radar, is one technology that offers the possibility to measure vertical ground movement [10,11]. It is a form of radar imaging used to create detailed images of landscapes and objects and provide detailed information on ground deformation, allowing for the detection and geodetic measurement of SVGM with unprecedented accuracy [12] and with a high spatial and temporal resolution. It has an antenna system that sends electromagnetic pulses at an angle towards the Earth to create image strips that are about 100 km wide. By using two SAR images acquired either by two different antennas or by repeated passes, it is possible to use the phase measurements to determine the relative distance of an object as a fraction of the radar wavelength (in the case of repeated passes of the radar over the same area) and the difference in the sensor locations (in the case of the antenna(s) at different positions) to determine angular differences, which are useful for topographic mapping [13].

The superimposition of these images, known as interferometric SAR (InSAR), produces an interferogram that reveals the phase differences between the signals received by the radar instrument. This phase difference serves as an indicator of what has changed on the observed surface. Ignoring the impact of atmospheric delays during the travel of the signal, the phase difference is obtained from the contributions of the interaction of the signal with the ground surface, the satellite's position in orbit and the topography. By performing repeated passes over an area and multiple observations, these contributions can be modeled, allowing the phase difference to be modeled and enabling us to derive the expected surface change.

Several studies have established that the temperature, precipitation and drought have significant impacts on ground deformation patterns [14–16]. For instance, prolonged drought can induce subsidence due to soil compaction, while increased soil moisture during cooler seasons can lead to ground uplift [17–19]. However, these studies often focus on localized areas or the global scale [20–22]. Meanwhile, most studies found over Italy consider a local scale [23,24]. Studies addressing the relations between the climate variables (temperature, precipitation and drought) and SVGM have not been widely explored.

By using Spearman's rank correlation coefficient, this study aimed to quantify the correlations between drought conditions, temperature effects and ground deformation across Italy using the SVGM determined from InSAR data provided by the European Ground Motion Service (EGMS) for the period of 2018 to 2022. Specifically, drought conditions were assessed using the drought code (DC) from two sources: (i) the Copernicus Climate Change Service (C3S) Climate Data Store (CDS), labeled as DC_{CEMS}, and (ii) a 1-km-resolution DC map calculated ad hoc for this study, labeled as $DC_{1\mathrm{km}}$. The DC, traditionally used to infer forest fire risks, was used here as a proxy for drought due to the fact that the DC represents the condition of a layer that dries very slowly [25], with a time lag of ≈52 days [26]. This means that it reflects long-term drought conditions, which we hypothesize—together with the temperature—as having a significant correlation with SVGM, especially in areas of intense agricultural activity [27].

The main objectives for this study were as follows:

- to investigate the correlation between the SAR-derived SVGM and climatic conditions (drought and temperature) in Italy, examining whether drought events coincide with changes in surface elevation and ground motion patterns;
- to identify regions within Italy where SAR-derived land subsidence and drought conditions exhibit cluster patterns;
- to assess the implications of the identified correlation points and areas with specific causes;
- to analyze the influence of the thermal deformation effect on infrastructure due to temperature-induced vertical ground motion.

These are meant to offer insights into large-spatial-scale SVGM patterns and their correlations with climate variables across Italy.

2. Materials

2.1. Study Area

This study focused on Italy as the study area. The Italian territory is located in Southern Europe and stretches between longitudes 6° and 19°E and latitudes 35° and 47°N. In the north, Italy shares a border with France, Switzerland, Austria and Slovenia. The rest of the territory is surrounded by water, with the Adriatic Sea to the east, the Tyrrhenian Sea to the west and the Mediterranean and Ionian Seas to the south. Italy is characterized by diverse landscapes, featuring the Alps Mountains and the Po Valley in the north. The Po Valley, one of the most significant agricultural regions, is known for its fertile plains and dense urban centers, presenting an ideal study area due to these different land cover categories and its varied geology.

Italy's climate varies significantly across its regions, ranging from a humid subtropical climate in the north, influenced by the Alps and the Po Valley, to a Mediterranean climate in the southern coastal areas. There is also a different climatic scenario between the northern and southern regions, with the central part of the country, including Tuscany and Umbria, acting as a transitional zone between these two climatic zones. The north typically experiences colder winters and hot summers, while the south generally has milder winters and warmer temperatures throughout the year. For example, on a winter day, the temperature can vary greatly: it may be around −2 °C and snowing in Milan (north), 8 °C in Rome (central) and 20 °C in Palermo (south) [28]. This variation is often depicted on weather maps showing the temperature gradients across the country. Consequently, there is an associated trend in the loss of soil moisture and drought conditions across the country. Vertical ground deformation is a prominent issue in Italy, driven by factors such as the extraction of groundwater for agricultural and industrial activities, tidal influences (e.g., in Venice) and active volcanoes in the south [29]. Climate-related variables also have significant impacts across the region. For instance, in July 2022, there was an intense drought in Italy (Figure 1), the most severe drought that the country had experienced in 70 years, due to which the government declared a state of emergency in 5 regions in the northern territory (Emilia–Romagna, Friuli–Venezia Giulia, Lombardy, Piedmont and

Veneto). These climatic and environmental challenges make Italy a suitable area of interest for this research.

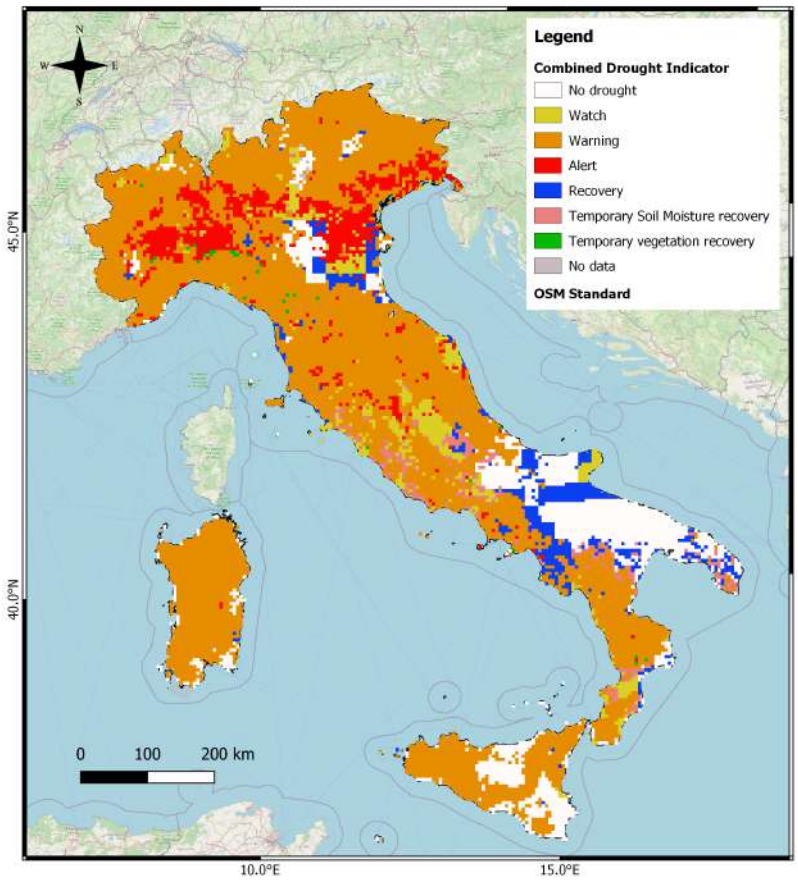

Figure 1. Combined drought indicators for the first 10-day period of July 2022 in Italy (JRC, 2024). This plot shows drought alert indicators over the northern regions, where a state of emergency was declared for this year. This event was an exceptional incident as, in general, the south of Italy is warmer than the north.

2.2. Data

The primary datasets utilized in this study are summarized in Table 1. These include (i) the European Ground Motion Service (EGMS) ground movement time series; (ii) land surface temperature (LST) data from the Moderate-Resolution Imaging Spectroradiometer (MODIS); (iii) precipitation data from the Climate Hazards Group Infrared Precipitation with Station Data (CHIRP) dataset; and (iv) the drought code from the Copernicus Emergency Management Service (CEMS) cems-fire-historical-v1.

Table 1. Data sources.

Source	Original Data	Spatial Resolution	Temporal Resolution	Reference
EGMS	Sentinel-1	100 m	6 days	[30]
MODIS product	MODIS Terra/Aqua	1000 m	Daily	[31]
CHIRP	Interpolation of precipitation stations	5566 m	Daily	[32]
CEMS Drought Code	Copernicus Service catalog	0.25° × 0.25°	Daily	[33]

3. Methods

This section describes the methods used to quantify the correlations between SVGM and the climatic variables, focusing on the use of Spearman's rank correlation coefficient (ρ) to assess the monotonic relationship between ground movement and the temperature

and drought code time series. The working diagram used for the method is provided in Figure 2.

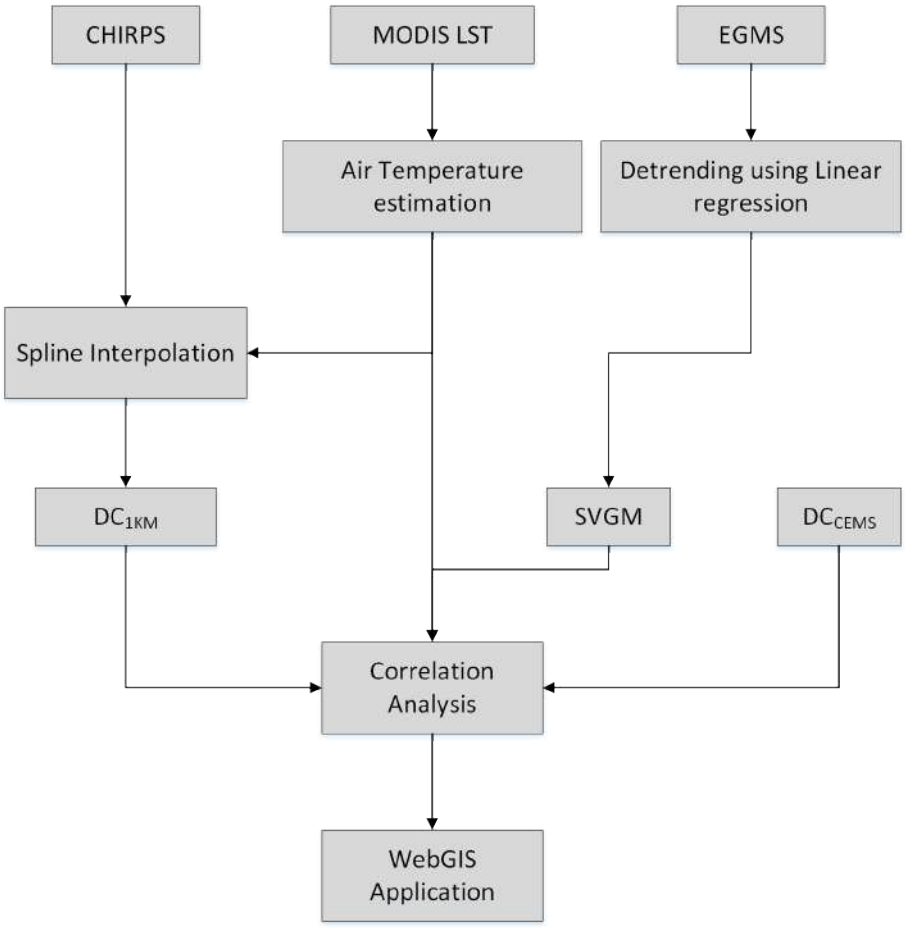

Figure 2. Flowchart of the methodology.

3.1. Drought Indices

Drought indices are tools used to quantify and monitor drought conditions by integrating weather variables, commonly the temperature and precipitation of the area of interest. These indices consider rainfall deficiencies over long periods that impact the moisture content of soils. In this work, we use the index known as the drought code (DC), developed from the original Drought Index of the Canadian Danger Rating Systems [34]. The original Drought Index had important limitations as its upper limit of 25 drying days was reached quickly during extended drying periods. The drought code (DC), which is used in this study, was developed from the stored moisture index (SMI) to overcome this limitation and is standardized with other indices. The drought code uses the temperature and precipitation and takes into consideration the number of drying days, e.g., days with no rainfall or no effective rainfall, i.e., only rainfall above 2.8 mm is considered effective [26,34,35]. This information is integrated with an estimate of evapotranspiration, which removes moisture from the ground. The DC index supports the estimation of various impacts of droughts on the Earth's surface. In this study, we use daily temperature and precipitation data to estimate daily maps of the DC values for the study area. The time series of these values are then used to calculate the correlations with SGVM.

3.1.1. Air Temperature Estimation

The MODIS Daytime Land Surface Temperature (LST) product (MOD11A1 V6.1) was used to estimate the temperature at the MPs' positions for the intended period and calculate the DC values (see Equations (1)–(6)). It must be noted that the LST and air temperature

are not equivalent, even if co-linear, and that there are different sets of spatiotemporal characteristics that distinguish them [36]. The LST refers to the temperature of the Earth's surface measured within a few meters above the ground surface. The air temperature, on the other hand, is measured at a height of approximately 1.5 to 2 m [37] above the ground. Using the LST as a proxy for the air temperature is reasonable, but it is not the ideal solution for the computation of the DC because it does not perfectly match the air temperature values. To correct for this, we applied a modeled correction factor from the work of [36]. The model from [36] allows one to estimate the air temperature from the LST and avoid errors when assuming that the LST and air temperature can be used interchangeably.

It should be noted that temperature rasters have a number of gaps in time and space due to low-quality pixels, usually from clouds or other limitations due to the atmosphere or from sensor malfunctions. To fill these gaps, spline interpolation was applied to estimate the values in empty cells. The final product is a continuous map at a 1 km resolution of the daily temperature for the 5-year period considered in this study. The map is available for download [38].

3.1.2. Precipitation

The daily precipitation estimated values were obtained from the CHIRPS dataset. The CHIRPS dataset is a global rainfall dataset provided by the United States Geological Survey and the Climate Hazards Center. It incorporates 0.05°-resolution satellite imagery (which is based on infrared cold cloud duration observations) with in situ station data to create gridded rainfall time series using interpolation approaches [32]. It is available on a daily, monthly or seasonal basis and also useful for performing trend analysis and seasonal drought monitoring, making it valuable for this work. From the validation performed by the authors, we can expect a global correlation of 0.69 and a mean absolute error of 82 mm [32]. Validation was carried out also in the African continent, not too far from our region, with results of a 0.6 correlation and 79 mm mean absolute error [32]. The dataset was clipped to the study area, exported and used for the estimation of the drought code.

3.1.3. Drought Code (DC)

The drought code is an indicator of the moisture content in deep compact organic layers. This code represents a fuel layer approximately 10–20 cm deep. The drought code fuels have a very slow drying rate, with a time lag of 52 days. The drought code scale is open-ended, although the maximum value is about 800 [39]. In this work, two versions of the drought code maps are tested. One is the reanalysis dataset with a grid cell resolution of 0.25° (≈20 km) provided by the Copernicus CEMS: cems-fire-historical-v1. This will be referred to as DC_{CEMS}. The other version of the drought code map was computed ad hoc with a spatial resolution of 1 km. This was estimated using the precipitation and temperature datasets described in Sections 3.1.2 and 3.1.1, respectively, and will be referred to as DC_{1km}.

DC_{1km} was calculated based on rainfall values from CHIRP on the day (DC_t) and the DC value of the previous day (DC_{t-1}) with the following equations [40]: Equation (1) in case of rainfall equal to or above 2.8 mm, and Equation (5) in case of lower rainfall values. If the rainfall is equal to or above 2.8 mm, it is considered effective rainfall, and the following equations are then used to update the DC value with respect to the DC value of the previous day:

$$DC_t = 400 \times ln(800/Q_t) \quad (1)$$

$$Q_t = Q_{t-1} + 3.937 \times r_e \quad (2)$$

$$Q_{t-1} = 800 \times e^{-DC_{t-1}/400} \quad (3)$$

$$r_e = 0.83 \times r_t - 1.27 \quad (4)$$

where

DC_t is the drought code from the rainfall data of the current day;

DC_{t-1} is the drought code of the previous day;
Q_{t-1} is the moisture equivalent of the previous day;
Q_t is the moisture equivalent of the current day;
r_t is the rainfall of the day in mm from the CHIRP dataset;
r_e is the effective rainfall.

In the case of rainfall below 2.8 mm, the DC value for the day is updated based on the temperature at midday and DC_{t-1}, i.e., the DC code of the previous day, with the following equations:

$$DC_t = DC_{t-1} + 0.5 \times V \quad (5)$$

$$V = 0.36(T_{12} + 2.8) \times L_f \quad (6)$$

where

$\boldsymbol{T_{12}}$ is the temperature at midday—here, it is estimated from the MODIS LST and converted to the air temperature by a factor of 0.74, as documented;
$\boldsymbol{L_f}$ is a day-length factor, which is constant for each month and is −1.6 for the months of November through to March and 0.9, 3.8, 5.8, 6.4, 5.0, 2.4 and 0.4, respectively, for the months from April to October;
$\boldsymbol{V}$ is the potential evapotranspiration.

3.2. Seasonal Vertical Ground Movement Estimation

The EGMS is one of the 6 main Copernicus Land Monitoring Services and uses InSAR data derived from Sentinel-1 to detect and measure ground movement across Europe with millimeter precision. It provides 3 main InSAR products: basic (LEtVEL 2a), calibrated (level 2b) and ortho (level 3). A summary of these product categories is provided here, and further details can be obtained from the technical report [41].

3.2.1. Basic EGMS Product

The EGMS basic product provides displacement measurements along an imaginary line—referred to as the line of sight (LOS)—connecting the satellite to the ground target, referred to as the measurement point (MP). The displacement along the line of sight is reprojected to derive the vertical/horizontal displacement at the MP. These products are also provided from SAR data acquired orthogonal to the ascending or descending trajectory of the satellite. The basic products are spatially referenced to a virtual reference point (whose time series is derived by a statistical analysis of the dataset) and temporally referenced to an initial starting time (T_0 = 0).

Each basic product uses a virtual reference point derived from the statistical analysis of the dataset within its specific processed area. Thus, the reference point might vary for different products or even for the same area. Thus, a direct comparison between different products of this level might produce inconsistent results, as the displacement measurements are relative to their own reference points.

3.2.2. Calibrated EGMS Product

The EGMS calibrated product is an advanced version of the basic product in which displacements are measured with reference to an Earth-centered reference frame model derived from GNSS time series data, thereby making the measurements absolute. Thus, a result that is more consistent would be obtained when comparing different products of displacement from the same or adjacent areas. However, GNSS data might not be available for some areas, especially isolated islands. In this case, the basic products are harmonized with each other and the mean ground velocity is adjusted to zero, making the measurement internally consistent and comparable within the local context using the InSAR data. The calibrated products are also provided from SAR data acquired orthogonal to the ascending or descending trajectory of the satellite.

3.2.3. Ortho EGMS Product

The EGMS ortho product exploits measurement of displacement from the calibrated products, breaking it down into two components (vertical and east–west displacements), resampled to a 100 m grid to coincide with the other Copernicus products. This simplifies the interpretation of the data as it eliminates the need to consider the original geometry of the satellite data acquisition. It also allows the interpretation of the displacement along a particular direction (for instance, in the case of a landslide).

Among others, the ortho product has the limitation that the Sentinel-1 satellite uses a side-looking radar in a near-polar orbit. Thus, the radar is less sensitive to ground displacements along the satellite's flight path (i.e., in the north–south direction). As a result, MP displacements in the north–south direction will not be measured directly by InSAR but inferred from the GNSS data introduced in the calibrated products [41]. Since GNSS data have a lower spatial resolution compared to InSAR measurements, displacements along the north–south direction are estimated through spatial interpolation from the available data.

For this study, the EGMS ortho product was used due to the advantages that it offers. Each EGMS tile that covers land contains approximately 150,000 MPs; 92 tiles were used to cover the study area. Each measurement point was a vector with a time series of ground displacement values, measured approximately every 6 days. For the 5-year period being considered for this study (2018–2022), about 300 observations for each MP were available. The corresponding DC values at each point were obtained using the Copernicus CEMS data (DC_{CEMS}) with a 0.25° resolution and our own data calculated from the MODIS and CHIRP ($DC_{1\text{km}}$) datasets. The Spearman rank correlation, *p*-value and confidence interval were the results used to assess the correlation at each MP between the seasonal patterns of ground vertical movement and the drought and temperature.

3.3. Assessment of Correlations Between SVGM and Climate Indices

Climate-driven correlations with seasonal vertical ground movement (SVGM) from InSAR were the focus of the analysis in this work. By "seasonal", we mean that the uplift and subsidence of the ground level follow a periodic pattern, repeating every year. To assess the correlations with climate indices, the data of EGMS ground displacement are detrended over the whole monitoring period using a linear regression approach. This is necessary to remove long-term trends in the time series of the ground movement for each measurement point (MP). The goal was to assess the SVGM in terms of recurring patterns (harmonic patterns) and determine whether these patterns are correlated with the climate. This analysis was carried out at the locations of all MPs recorded by the EGMS ortho product. The proxies used for the climate were the two drought code maps (DC_{CEMS}, $DC_{1\text{km}}$) and the temperature from MODIS.

Spearman's rank correlation coefficient was calculated at each MP. The Spearman correlation is more robust, with respect to Pearson's correlation, to relations that are not linear throughout the range of values. Both positive and negative correlations were considered. A positive correlation was noted when there was ground uplift with higher values of the compared independent variables (DC_{CEMS}, $DC_{1\text{km}}$ and temperature). A negative correlation occurred when the ground subsided and the climate index values increased. Both behaviors have been observed and documented in the past scientific literature. For instance, a positive correlation is often found in cases where infrastructure exhibits seasonal expansion due to thermal effects [42].

3.4. Development of WebGIS Application

As a side product of this research, a WebGIS application was developed in R using the Shiny and Leaflet libraries to interactively visualize the spatial distribution of the MPs. This application was developed to serve as a platform for the visual inspection of the spatial and temporal correlations between SVGM and the climate-related variables at the MPs. It is available for the detection of hotspots of the phenomenon of climate-driven SVGM and for further analysis.

3.5. Development of Intermediate Data Products

An intermediate data product was developed at a ground sampling distance of (≈1 km) by regridding the datasets used for this study. Further details of these products are provided in Section 4.3. It should be noted that the EGMS data cover 1 January 2018 to 17 December 2022. The data layers calculated for this study start from 2017, one year before the EGMS data (2018), because the DC calculation requires the precipitation and temperature information from previous days to be reliable. Thus, the first few months of 2017 were estimated for the accurate calculation of the $DC_{1\text{km}}$ layer, but only the ones from 2018 to 2023 were used, to match the EGMS data's temporal coverage.

4. Results

The Spearman rank correlation, *p*-value and confidence interval values are reported in the following sections in order to assess the resulting relationships between the seasonal patterns of ground vertical movement and the drought and temperature at each MP.

4.1. InSAR Seasonal Vertical Ground Movement Correlations

The ortho product of the EGMS provides an RMSE for each measurement; we therefore analyzed the distribution of the RMSE for all points used and provide the distribution of expected accuracy. The resulting distribution of the RMSE for the percentiles 1%, 10%, 25%, 50%, 75%, 90% and 99% is, respectively, 0.5 mm, 0.7 mm, 0.9 mm, 1.4 mm, 2.2 mm, 3.0 mm, 4.2 mm. The vertical ground movement detected is a degree of magnitude larger than the accuracy values; thus, we can safely conclude that the observations are reliable. The correlation results were tested for significance, and all *p*-values were <0.01.

The results of the seasonal correlation patterns using Spearman's rank correlation coefficient (ρ) between the ground vertical motion and DC_{CEMS}, $DC_{1\text{km}}$ and temperature show a significant number of points with strong correlations, both negative and positive. The total number of MPs over Italy is 7,193,676. The total number of correlated points is 32,826, amounting to about 0.46% (Table 2). It is clear that only a minor proportion of the points are correlated. Figure 3 shows the distribution of the (ρ) values for all MPs over the study area [1].

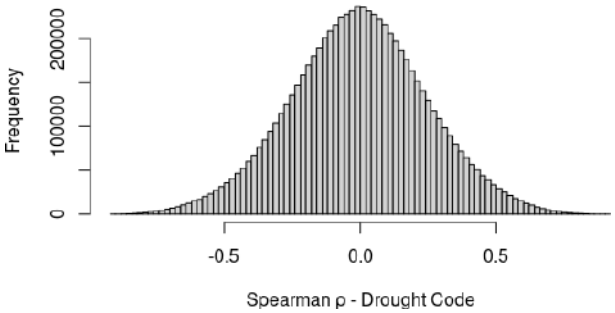

Figure 3. Histogram of frequency distribution of Spearman correlation values (ρ) between $DC_{1\text{km}}$ and SVGM at MPs [1].

Table 2. Number of MPs with strong correlation between SVGM and climate variables considered.

Climatic Factor	Positive ρ	Negative ρ	Total
DC_{CEMS} $\lvert\rho\rvert > 0.7$	5868	13,511	19,379
DC_{CEMS} $\lvert\rho\rvert > 0.8$	220	1529	1749
DC_{1km} $\lvert\rho\rvert > 0.7$	12,142	20,684	32,826
DC_{1km} $\lvert\rho\rvert > 0.8$	1275	2594	3869
$Temperature$ $\lvert\rho\rvert > 0.7$	6819	3538	10,357
$Temperature$ $\lvert\rho\rvert > 0.8$	3727	548	4275

From Table 2, it can be seen that a total of 1275 MPs have positive correlation coefficients between the DC_{1km} map and SVGM measurements above 0.8, and 2594 have ρ below −0.8 (negative correlation). Correlations that lagged in time were also analyzed, where it was observed that most of the correlated MPs had stronger correlations on the day for which they were calculated (0-day lag time, Figure 4).

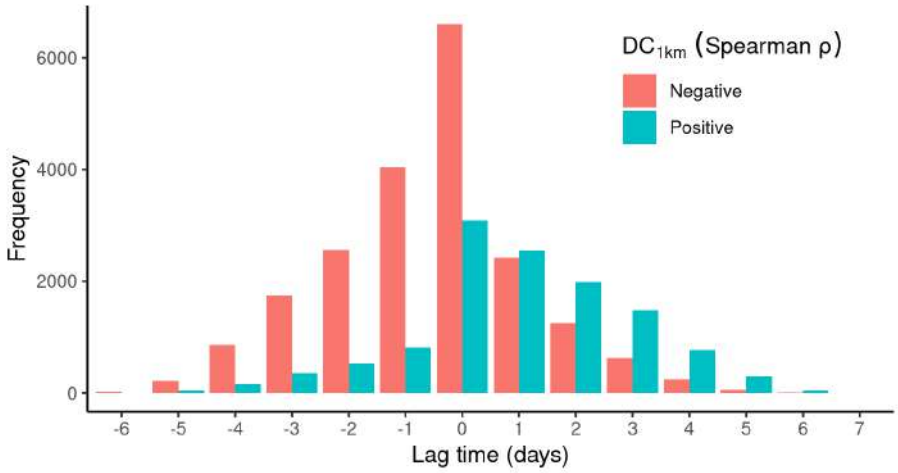

Figure 4. Lag time distribution of best correlations between DC_{1km} and SVGM [1].

The above observation does not hold true for the temperature, where the lag time improves the correlation significantly. Figure 5 shows that a month's negative lag time gives the best correlation for negatively correlated MPs.

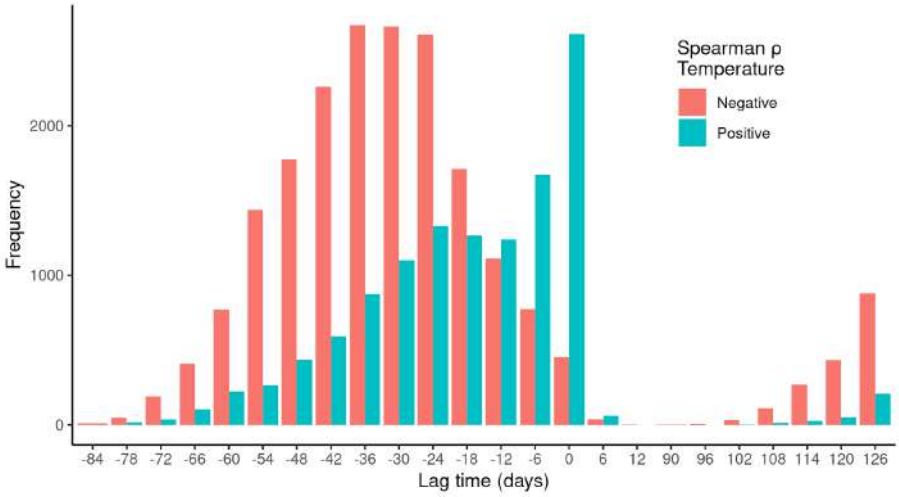

Figure 5. Lag time distribution of best correlations between temperature derived from calibrated MODIS and SVGM [1].

4.1.1. DC_{CEMS} vs. DC_{1km}

The initial results over Italy show that DC_{1km} is significantly more correlated with SVGM than DC_{CEMS}, with a stronger median absolute value of ρ of 0.025 and 0.042, respectively, for negative and positive correlation scenarios. Figure 6a shows this difference, as the scatter points are mostly on the right of the 1:1 diagonal line for negative correlations and vice versa for positive correlations. This means that most points with a negative correlation regarding ground motion patterns with respect to the DC, show that, for $DC_{1km} - DC_{CEMS}$ pairs, DC_{1km} is usually more negative (stronger negative correlation). The opposite is true for positive correlation scenarios. The Kruskal–Wallis pairwise difference of medians provides a ρ-value of a significant difference <0.001.

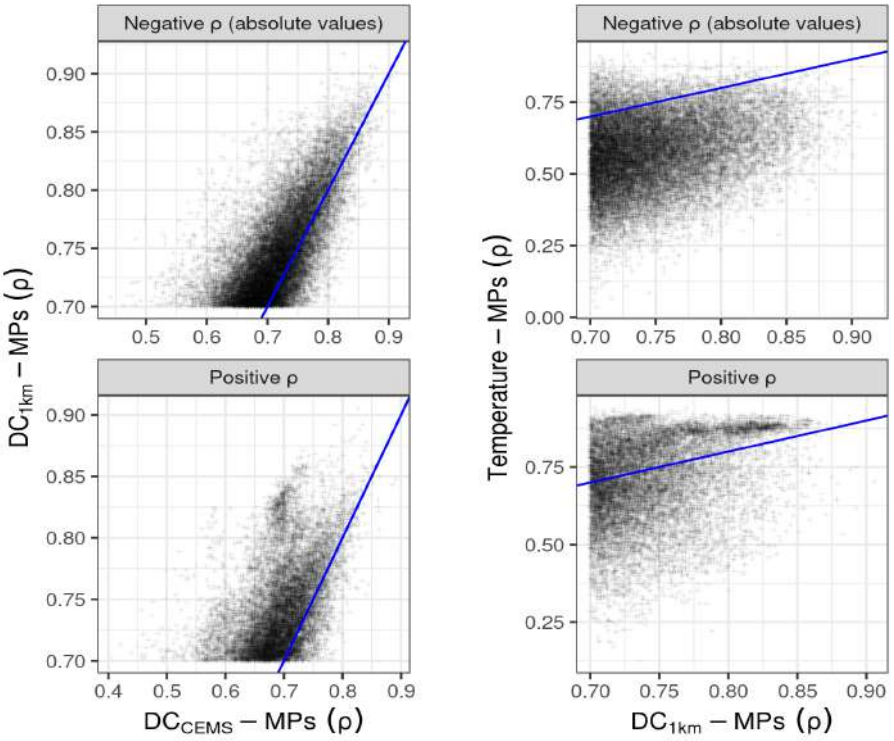

(**a**) (**b**)

Figure 6. (**a**) Pairwise DC_{CEMS}–DC_{1km} values of correlations with ground motion; (**b**) temperature vs. DC_{1km} correlation. Top and bottom rows are negative and positive (ρ) values from correlation testing with SVGM [1].

4.1.2. DC and Temperature

Because the DC and temperature are strongly collinear, further analysis to assess which is more applicable in explaining the seasonality of ground motion was carried out. The results shown in Figure 6b indicate that DC_{1km} explains significantly more variance than the temperature if we consider negative correlations. This is clear as most points fall below and to the right of the blue line, which represents the 1:1 perfect correspondence of the ρ values for the temperature and DC_{1km} at each MP. This can be interpreted as indicating that most MPs have seasonal vertical movement that is better represented by DC_{1km} than the temperature for negative correlations. A positive correlation with SVGM does not result in such a prominent difference between the temperature and DC_{1km}.

The plots in Figure 6 above provide information on the higher sensitivity of DC_{1km} in detecting seasonal ground movement with respect to DC_{CEMS}, as the pairwise comparison from the scatter plot shows consistently higher correlation values when using the DC_{1km} data rather than the DC_{CEMS} data. If we compare the temperature and DC_{1km}, as in the second column of the plot, we see that the temperature is a better indicator (stronger correlations) of ground movement in its positive correlation than DC_{1km}, but this is not true for negatively correlated measurement points.

4.2. Spatial Distribution of MPs in Italy

Figure 7 shows the overall spatial distribution of the MPs with significant positive and negative correlations. The top row shows hexagonal cells with a 10 km diameter with the percentage of EGMS MPs that have values of ρ above or below 0.7. The bottom row shows the hotspots in Italy that have a very large number of MPs with positive correlations and are thus worth further investigating.

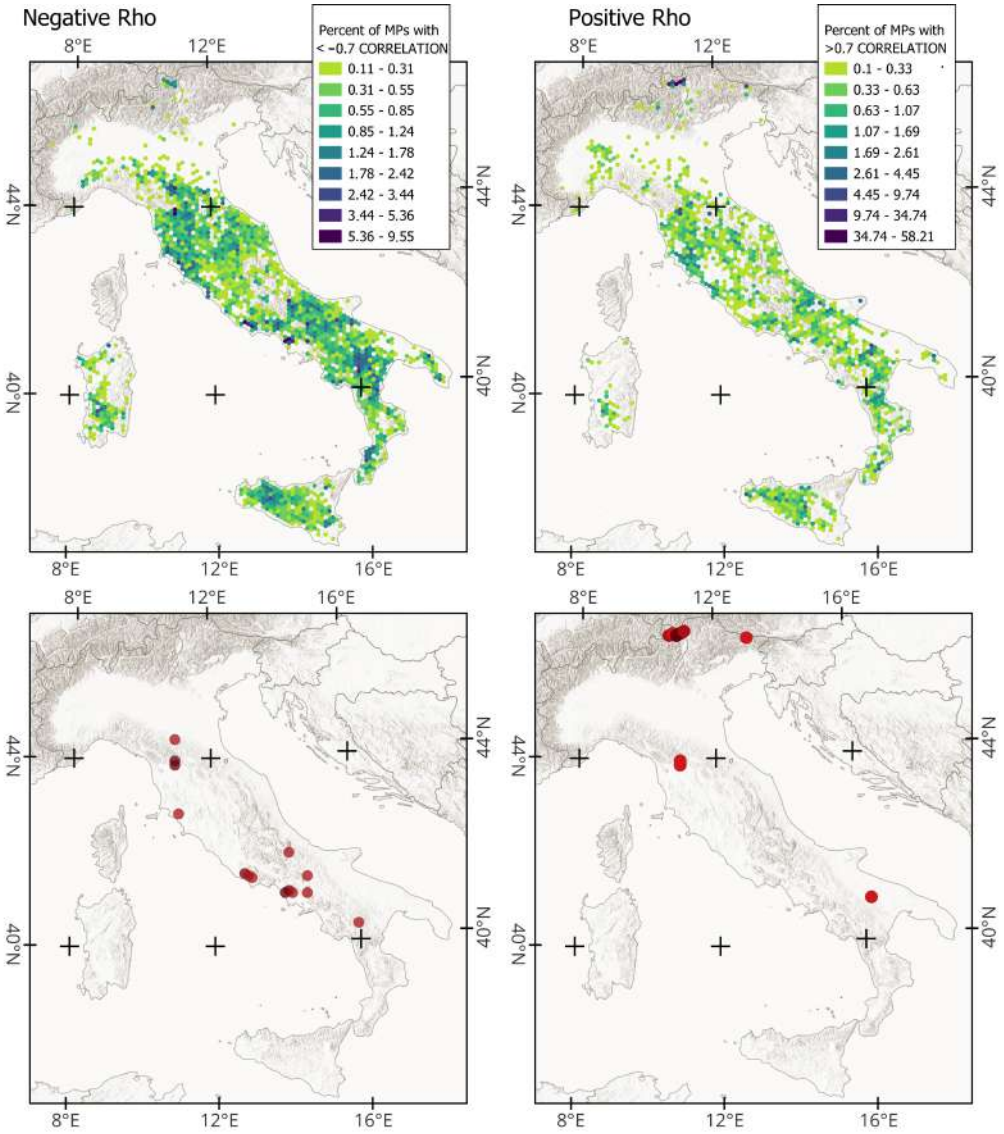

Figure 7. Top row shows the spatial distribution of negative and positive correlations (**left** and **right**) in terms of the percentage of correlated MPs with respect to the total number of MPs recorded by the European Ground Motion Service. The percentage was calculated over a regular hexagon grid overlaid onto the study area. Bottom row pinpoints areas (red dots) with the highest percentage of correlated MPs, negative (**bottom-left**) and positive (**bottom-right**).

4.3. Data Availability and WebGIS Data Viewer

An open dataset consisting of three raster grids and a vector of MPs was an intermediate result from this study. These data are available publicly to provide a replicable methodology and share them with other investigators [38]. The layers in the dataset are the following:

1. grid with daily precipitation (mm);
2. grid with daily air temperature interpolated values (°C);
3. grid with calculated drought code DC_{1km} (no unit);
4. point vector with extracted MPs with correlation ($|\rho| > 0.7$).

The first three datasets have one band per day from 1 January 2017 to 1 January 2023, for a total of 2192 bands. All data are given in geographic coordinate systems using the WGS84 system and aligned to an extent of 6.6116°, 18.51428°, 35.48345°, 47.09867°, with a ground sampling cell distance of $8.983153° \times 10^{-3}$ (≈1 km). All four data layers are

available as per the F.A.I.R. (Findable, Accessible, Interoperable and Reusable) guiding principles for research data stewardship and are provided in open-access format—see [38].

The developed WebGIS application presents a map of the MP stations and has tools for user interaction with the map. Upon clicking on an MP, a pop-up window is displayed, showing the following attributes for the DC_{CEMS}, DC_{1km} and temperature variables, in addition to the longitude (φ) and latitude coordinates (λ) of the MP stations (see samples in Figure 8):

- coordinates of MP;
- Spearman's rank correlation (ρ);
- confidence interval;
- highest ρ at lagged time;
- lag (days).

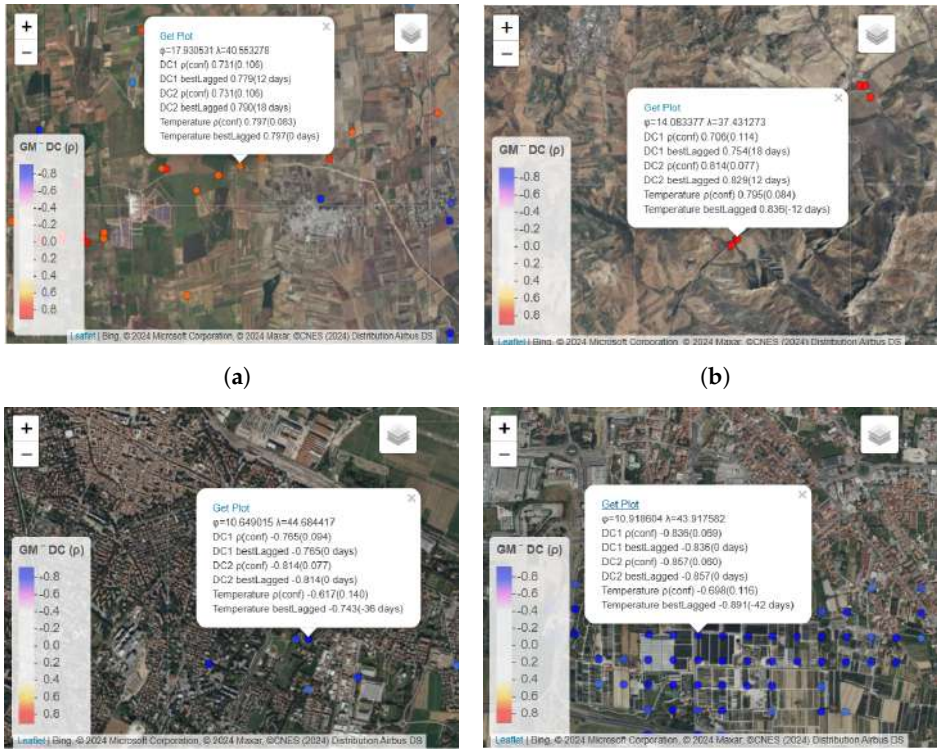

Figure 8. Measurement points with positive (**a**,**b**) and negative (**c**,**d**) Spearman correlation values.

Figure 9 also shows the time series plots that can be automatically extracted by the user at selected MPs. These are useful for further exploratory analysis.

The objective of this work was to detect and analyze MPs that exhibit a significant correlation among periodic ground movement, drought and the temperature. Spearman's rank correlation coefficient ρ was calculated for all MPs and a threshold was applied to filter the MPs that had an absolute Spearman's rank correlation coefficient ρ above 0.7. This threshold was necessary to focus the analysis on the MPs that had higher values of positive or negative correlations between the climate variables and SVGM. In the web application, it is, however, possible to vary the threshold to isolate MPs using more stringent threshold values.

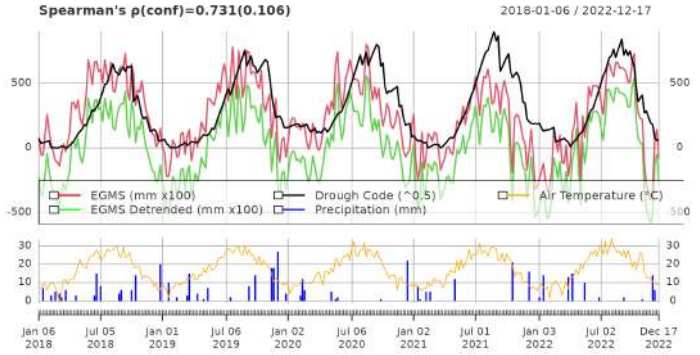

(**a**)

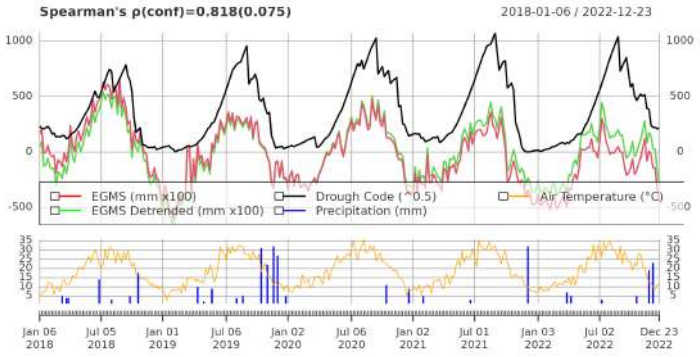

(**b**)

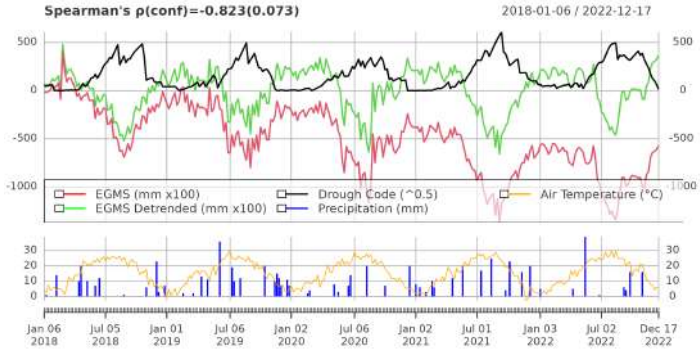

(**c**)

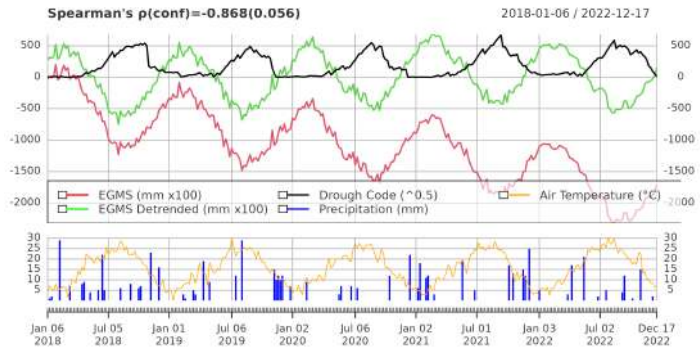

(**d**)

Figure 9. Time series plot showing the correlations at the respective measurement points in Figure 8.

4.4. Analysis at Selected Measurement Points (MPs)

Figure 8 shows the display of the pop-up menu of the WebGIS over four MP locations chosen over the area: the top row shows two locations that exhibit positive correlations

and the bottom row shows two locations having a negative correlation. Figure 9 shows the time series plot of these variables at the selected MPs.

In Figure 8, at the top left, an MP exhibiting a positive correlation is depicted from an open field in the Brindisi region, close to Tuturano, in the southeastern part of Italy. In this example, a positive correlation of ρ = 0.731 was observed for both DC_{CEMS} and DC_{1km}, with a small increase with a lag time of 12 and 18 days, respectively. The temperature correlation was, however, stronger than that of the DC at a value of ρ = 0.797 and there was no improvement with the lag. The improvement from the lagged correlation found with DC values and the best correlation with the temperature found at zero lag indicate that the SVGM is likely driven more by the temperature than drought. Further visual analysis shows that similar scenarios are found in areas where large electrical pylons are installed. Another group of MPs where a strong positive correlation was observed was located near the Besaro bridge, located in the Caltanissetta region in the south of Italy (Figure 8, top right). These points were considered due to the potential impact of the correlation on the analysis of road infrastructure.

As an example of a negative correlation, two areas are shown in the bottom row of Figure 8—one in Via Bonellina in the Province of Pistoia (bottom left) and one in Orti sociali Spallanzani (Via Arturo Toscanini) in Reggio Emilia (bottom right), all in the northern sector of the territory—where a strong negative correlation was seen. The selected MPs were in agricultural areas that were approximately 87.9 km apart.

5. Discussion

In this study, we analyzed the correlations between SVGM, the temperature and two drought code (DC) maps—one derived from Copernicus data with a 20 km cell ground sampling distance (referred to as DC_{CEMS}) and the other calculated from the MODIS and CHIRP datasets at a 1 km resolution and on a daily basis (referred to as DC_{1km}). It is worth noting that the EGMS data have a grid with nodes at every 100 m, whereas the DC_{1km} grid has nodes at every 1 km; thus, approximately 100 EGMS points fall within a single DC_{1km} cell. Downscaling to match the EGMS resolution could be explored, and methodologies such as those discussed in [43] could be applied to enhance the precision.

The finer resolution of the locally generated drought codes (DC_{1km}) provided a larger number of correlated MPs with SVGM than the coarser DC_{CEMS}. This is particularly true for MPs showing positive correlations, where DC_{1km} exhibits twice as many MPs with a correlation >0.7 and five times the number of MPs with a stronger correlation with ground movement of $\rho > 0.8$. This result suggests that the higher spatial resolution of DC_{1km} allows the capture of more localized variations in the drought conditions.

There is a strong connection between drought and the temperature. High temperatures increase the evaporation rates, which increase the drought effects by reducing the available soil moisture and drying out the soil [44]. Climate change is also another factor as it is expected to increase the frequency and intensity of droughts in many parts of the world, due to rising temperatures [45]. Section 4.1.2 reveals that the temperature tends to have a more significant impact on SVGM, especially in areas showing positive correlations. However, in regions with negative correlations, the drought code appears to better explain the observed ground movement.

5.1. Thermal Deformation of Infrastructure

The observed positive correlations at pylons and bridges, as can be seen in the results in Figure 9, all range within ±5 mm; thus, there is an overall 1 cm deformation range, and this might be attributed to the thermal deformation of the considered infrastructure. The assumed thermal deformation of steel and/or concrete infrastructure is supported by the results of other studies. For example, the work of [46] shows that the amplitude increases from 0.5 mm/°C at 50 m for buildings that are about 250 m high to 1.0 mm/°C for buildings that reach a height of 345 m, as shown in Figure 5 in [46]. If we consider the large electricity pylons to be approximately 50 m high, and a reasonable air temperature

difference between seasons of 30 °C, we would obtain a 1.5 cm deformation. This is similar to our 1 cm observed pylon deformation. The difference is likely due to the different compositions of the infrastructure, as pylons are fully metallic and are also less tall than the buildings considered in [46].

For further visualization, Figure 10 shows the specific scenario of a highway overpass, with a central pillar of a known height (172 m). This has a seasonal deformation of +2.5 cm in summer and −1.0 cm in winter, for a total range of approximately 3.0 cm. This is more comparable to the measured smaller building in [46], where an approximate expansion of 1.5 mm/°C was observed at 175 m. Again, this would result in this deformation being caused by an air temperature difference of 20 °C, which is reasonable considering the region. Downward vertical ground movement caused by land subsidence might be combined with upward movement from the expansion of infrastructure [47]. This is true if we consider the long-term overall vertical movement, but it should be eliminated by detrending for the long-term trend.

Figure 10. "Viadotto Gorsexio" with a central pillar taller than 172 m.

5.2. Spatial Analysis of the Correlations at the MPs

The spatial distribution of MPs with significant correlations, as shown in Figure 7, shows how the correlations between the climate variables and SVGM vary with space in the study area. Figure 7 shows the spatial distribution of the measurement points that have strong correlations with seasonal vertical ground movement—in other words, points where the Earth's surface's vertical movement is in relation to the temperature or drought conditions. This is intended to provide insights into where this phenomenon is occurring and thus indicate a direction for further research. By adding the points in the bottom row, we illustrate the hotspots of strong seasonal positive and negative correlations with climatic factors. This correlation is, however, not uniform across the study area. Moreover, the concentration of MPs with higher absolute values of correlation (positive or negative) in certain areas suggests that localized factors might be influencing the relationship between the SVGM and the climate variables. These factors might be natural (e.g., soil composition, vegetation) and/or anthropogenic (e.g., infrastructure, land use), being specific to the given area, although more complex phenomena can arise from the complex geological system of the area [3]. For instance, in the study of [48,49], it was found that the geological structure of an area, such as the orientation of rock discontinuities, can drive ground deformation in the area. Figure 7 shows that a small percentage of the total number of MPs measured by the Copernicus EGMS have correlations and that only a limited number of areas have clusters with many MPs having correlations, as shown in the bottom row of Figure 7. This is expected due to the localized factors playing an active role in driving the correlation between the SVGM and the climate variables. The figure also shows gaps in the northern part of Italy, which is characterized by flat landscapes, and this might be due to the weaker effects of the climate on ground deformation or to a surface that is less responsive to climate-induced deformations.

The selected MPs in Section 4.4 demonstrate contrasting scenarios of positive and negative correlations, providing insights into how the climate variables, driven by site-specific conditions, such as the presence of infrastructure or geological characteristics, drive vertical ground movement.

For instance, the positive correlations at Brindisi and the Besaro bridge suggest that the thermal deformation of infrastructure at these sites plays a significant role, as the correlations due to the temperature are generally stronger than those due to the drought code. Moreover, the lag times of the temperature are very low compared to those of the drought code at these stations, suggesting that the temperature has an immediate impact on the vertical ground displacement at these sites compared to the drought code due to the infrastructure's presence. Conversely, negative correlations are observed at the MPs in the agricultural fields in Pistoia and Reggio Emilian, where the drought codes have stronger correlations and low lag times compared to the temperature, suggesting that the changes in vertical ground displacement are driven by the drought code in these areas. This might be attributed to the irrigation practices in these agricultural areas. This is supported by the fact that irrigation causes the volumetric deformation of soil particles [50], which then impacts the vertical displacement of the ground surface.

Moreover, the 0.4% of the MPs where a correlation between the climate variables and SVGM is observed indicate that, while climate variables influence SGVM, it is not uniform across the study area, as observed in Figure 7. This is worth considering for future studies, as there has not been any study assessing the correlation between SVGM and the selected climate variables to a larger extent, to the authors' knowledge.

5.3. Lag Time Analysis

The lag time analysis (Figures 4 and 5) provides critical insights into the temporal dynamics of these correlations. The observation that most MPs show the strongest correlation at zero lag time for the DC but a significant lag for the temperature suggests that different processes are at play. For instance, the temperature might influence ground movement with a delay [51], as thermal effects on soil or rock take time to manifest fully, whereas the impact of drought on the ground conditions might be more immediate.

5.4. Infrastructure Monitoring

Figures 10–12 show the specific scenario of a highway overpass, "Viadotto Gorsexio", with a central pillar of a known height (172 m). This has a seasonal deformation of +2.5 cm in summer and −1.0 cm in winter, for a total range of approximately 3.0 cm. This is more comparable to the thermal deformation of smaller buildings as studied in [46], where an approximate expansion of 1.5 mm/°C was observed at 175 m. This would imply that the 3.0 cm deformation of the structure is caused by an air temperature difference of 20 °C, which is reasonable considering the region in which the structure is located.

Figure 11. Display of information related to EGMS and climate correlation values of the area in the WebGIS viewer.

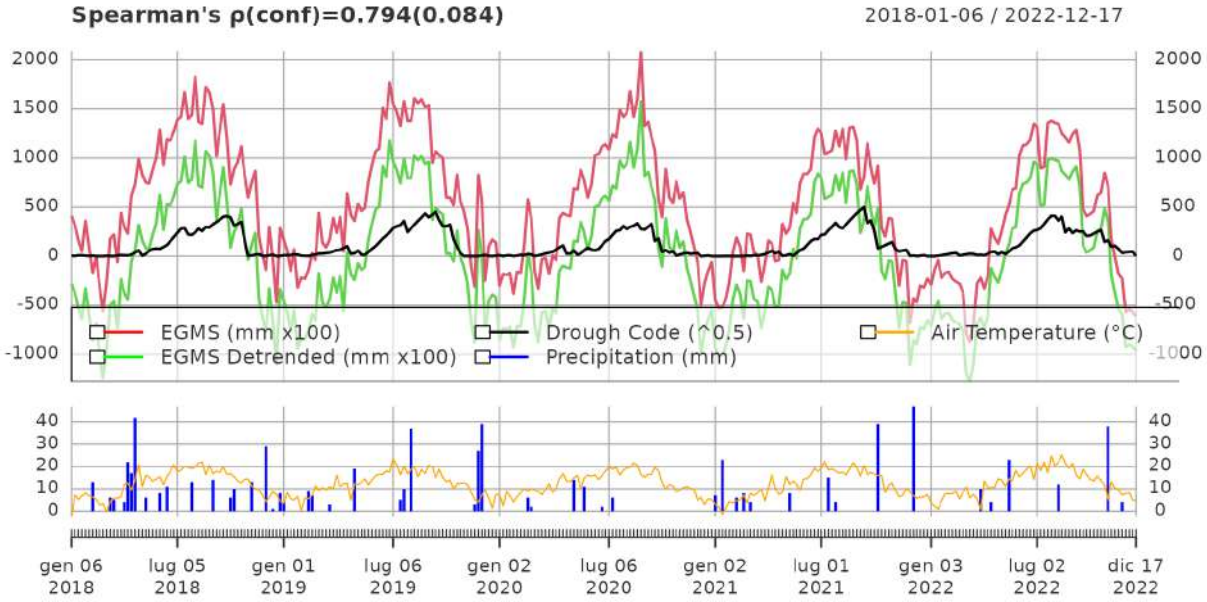

(**a**)

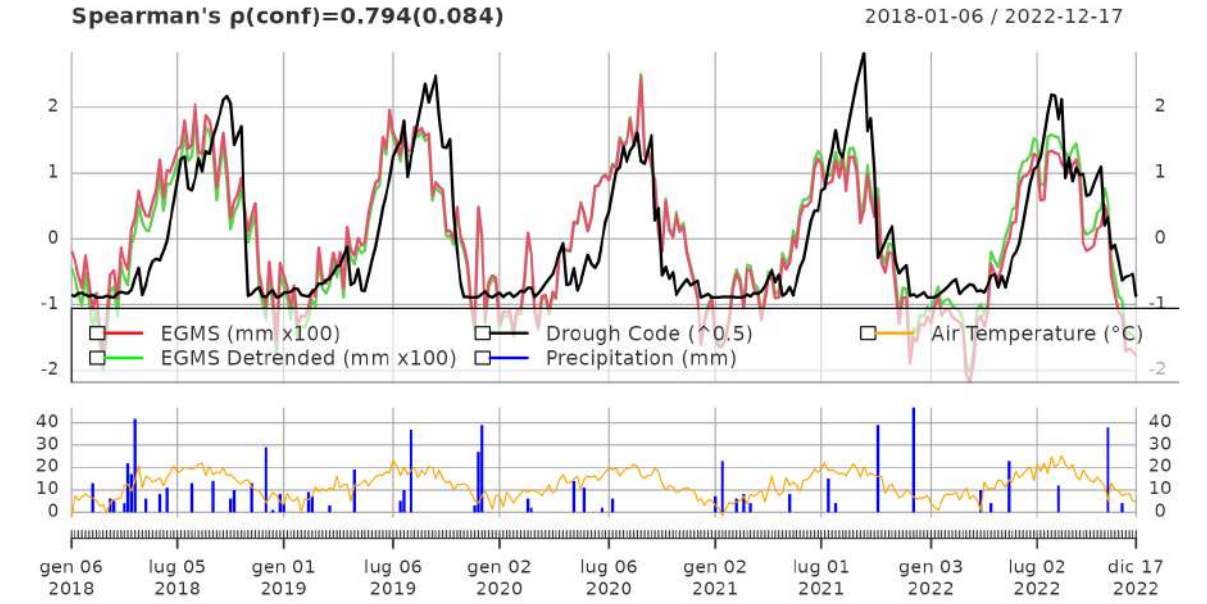

(**b**)

Figure 12. Time series plot of the corresponding correlation (**a**) and the same time series with normalized values (**b**).

The correlation value observed at an MP on the pillar for the temperature was $\rho = 0.860$, higher than the one from DC_{1km} ($\rho = 0.793$). This is evident in Figure 10, as it is a very high bridge with a central pillar taller than 172 m. This is also evident in the right-bottom panel of Figure 6, which shows that the temperature correlations are stronger (above the black 1:1 line) than those for the DC.

5.5. Limitations of the Research

The correlations between SVGM, the temperature and the DC are affected by the land cover, e.g., road infrastructure and agricultural areas, because the dynamics are very different with regard to the behavior of thermal expansion, i.e., for infrastructure with tall elements, and the mixed behavior of the ground, which can combine subsidence from water

table depletion and ground uplift from increased moisture content in the soil. Moreover, the latter depends on the type of soil and, of course, the ground vegetation cover. It can also be noted that spurious correlations are possible in time series, but the probability of a consistent seasonal correlation being only due to chance is very low. It could be argued that the causality might be indirect and that the climatic indices used (temperature and drought) are "precursors" of more complex phenomena.

The pylons of electrical lines were seen to be strongly positively correlated with the temperature as they were expanded by heat due to their material and height, as in the literature reported. It is reasonable to suggest that some pylons might be located in areas that are subject to seasonal ground subsidence driven by drought, and these were thus not be detected in our analysis as these two phenomena cancel one another out. This aspect is worth considering in the future, as pylons act as important scatterers for the monitoring of ground movement using InSAR.

6. Conclusions

This study has investigated the correlations between seasonal vertical ground movement (SVGM) and temperature and drought conditions using InSAR data from the EGMS and drought codes derived from both the Copernicus and MODIS/CHIRP [38] datasets. The drought codes derived from the MODIS/CHIRP datasets generally show a stronger correlation with SVGM compared to the ones from Copernicus due to their higher resolution.

The spatial analysis of the MPs showed significant variability in the correlations across different regions, indicating that localized factors such as the soil composition, vegetation and infrastructure play a crucial role in driving SVGM. Additionally, the lag time analysis demonstrated that temperature effects often manifest with a delay at MPs with a positive correlation, whereas drought impacts are more immediate in areas with negative correlations. This highlights the complex interplay between the temperature and drought in influencing ground deformation.

The analysis at the selected MPs revealed that temperature variations significantly influence vertical ground movement in infrastructure, with the observed deformations ranging between ±1 cm and ±3 cm in some cases—for example, the "Viadotto Gorsexio" bridge. This confirms that thermal deformation [52] is a major factor that affects infrastructure.

The findings underscore the importance of considering both the temperature and drought conditions when monitoring and assessing infrastructure health. They will also be useful when designing policies to ensure sustainable land management practices in the face of changing climatic conditions. For instance, the observed correlations and deformation patterns provide valuable insights for the design and maintenance of infrastructure to withstand seasonal variations and climate-induced stresses.

Further analysis at a European scale will be performed to extend this study to a larger area. To better understand the area-specific factors driving SVGM, investigation at specific monuments will be required to understand some of the drivers of SVGM. Future research will also focus on exploring additional factors and assessing their correlations with SVGM.

Author Contributions: Conceptualization, methodology, (F.P.). Formal analysis, validation, review, investigation, original draft preparation, data curation (F.P. and F.E.T.). Review and visualization (A.G.). All authors have read and agreed to the published version of the manuscript.

Funding: This study was supported within the Agritech National Research Center and received funding from the European Union Next-GenerationEU (PIANO NAZIONALE DI RIPRESA E RESILIENZA (PNRR)—MISSIONE 4 COMPONENTE 2, INVESTIMENTO 1.4—D.D. 1032 17/06/2022, CN00000022)—task 4.3.1. This manuscript reflects only the authors' views and opinions; neither the European Union nor the European Commission can be considered responsible for them.

Data Availability Statement: The data that support the findings of this study are available as open data for download at https://zenodo.org/doi/10.5281/zenodo.12741043.

Conflicts of Interest: The authors declare no conflicts of interest.

References

1. Pirotti, F.; Toffah, F.E. Investigating the Relation Between Seasonal Vertical Ground Movement from InSAR and Environmental Variables. *ISPRS* 2024, *in press*.
2. Galloway, D.L.; Jones, D.R.; Ingebritsen, S.E. *Land Subsidence in the United States*; Number 1182 in USGS Circular; U.S. Geological Survey: Reston, VA, USA, 1999; p. 188.
3. Kanan, A.H.; Pirotti, F.; Masiero, M.; Rahman, M.M. Mapping inundation from sea level rise and its interaction with land cover in the Sundarbans mangrove forest. *Clim. Chang.* **2023**, *176*, 104. [CrossRef]
4. Bürgmann, R.; Dresen, G. Rheology of the lower crust and upper mantle: Evidence from rock mechanics, geodesy, and field observations. *Annu. Rev. Earth Planet. Sci.* **2008**, *36*, 531–567. [CrossRef]
5. Galloway, D.L.; Burbey, T.J. Review: Regional land subsidence accompanying groundwater extraction. *Hydrogeol. J.* **2011**, *19*, 1459–1486. [CrossRef]
6. Dzurisin, D. *Volcano Deformation: Geodetic Monitoring Techniques*; Springer-Praxis Books in Geophysical Sciences; Springer: Berlin/Heidelberg, Germany, 2007.
7. Alcoverro, J. The effective stress principle. *Math. Comput. Model.* **2003**, *37*, 457–467. [CrossRef]
8. Zhang, C.; Lu, N. Unified Effective Stress Equation for Soil. *J. Eng. Mech.* **2020**, *146*, 04019135. [CrossRef]
9. Welch, J.; Wang, G.; Bao, Y.; Zhang, S.; Huang, G.; Hu, X. Unveiling the hidden threat: Drought-induced inelastic subsidence in expansive soils. *Geophys. Res. Lett.* **2024**, *51*, e2023GL107549. [CrossRef]
10. Imai, H.; Ito, K.; Aoki, T.; Uemoto, J.; Uratsuka, S. A Method for Observing Seismic Ground Deformation from Airborne SAR Images. In Proceedings of the 2019 IEEE International Geoscience and Remote Sensing Symposium (IGARSS), Yokohama, Japan, 28 July–2 August 2019; pp. 1506–1509. [CrossRef]
11. Xu, Y.; Lu, Z.; Burgmann, R.; Hensley, S.; Fielding, E.; Kim, J. P-band SAR for Ground Deformation Surveying: Advantages and Challenges. *Remote Sens. Environ.* **2023**, *287*, 113474. [CrossRef]
12. Ferretti, A.; Passera, E.; Capes, R. End-to-End Implementation and Operation of the European Ground Motion Service (EGMS): Algorithm Theoretical Basis Document. Technical Report, Technical Report EGMS-D3-ALG-SC1-2.0-006. 2021. Available online: https://land.copernicus.eu/user-corner/technical-library/egms-algorithm-theoretical-basis-document (accessed on 10 April 2024).
13. Hanssen, R.F. *Radar Interferometry: Data Interpretation and Error Analysis*; Kluwer Academic Publishers: Dordrecht, The Netherlands, 2001.
14. Wang, Y.; Guo, Y.; Hu, S.; Li, Y.; Wang, J.; Liu, X.; Wang, L. Ground Deformation Analysis Using InSAR and Backpropagation Prediction with Influencing Factors in Erhai Region, China. *Sustainability* **2019**, *11*, 2853. [CrossRef]
15. Chaussard, E.; Milillo, P.; Bürgmann, R.; Perissin, D.; Fielding, E.J.; Baker, B. Remote Sensing of Ground Deformation for Monitoring Ground-Water Management Practices: Application to the Santa Clara Valley During the 2012–2015 California Drought. *J. Geophys. Res. Solid Earth* **2017**, *122*, 8566–8582. [CrossRef]
16. Tao, T.; Dai, J.; Song, Z.; Li, S.; Qu, X.; Zhu, Y.; Li, Z.; Zhu, M. Spatial-Temporal Dynamic Evolution of Land Deformation Driven by Hydrological Signals around Chaohu Lake. *Sensors* **2024**, *24*, 1198. [CrossRef] [PubMed]
17. Barthelemy, S.; Bonan, B.; Tomas-Burguera, M.; Grandjean, G.; Bernardie, S.; Naulin, J.P.; le Moigne, P.; Boone, A.; Calvet, J.C. Analyzing Past and Future Droughts that Induce Clay Shrinkage in France Using an Index Based on Water Budget Simulation for Trees. *EGUsphere* 2024, *Preprint*. [CrossRef]
18. Miller, M.M.; Jones, C.E.; Sangha, S.S.; Bekaert, D.P. Rapid Drought-Induced Land Subsidence and its Impact on the California Aqueduct. *Remote Sens. Environ.* **2020**, *251*, 112063. [CrossRef]
19. Zhou, X.; Zhang, S.; Zhang, Q.; Liu, Q.; Ma, Z.; Wang, T.; Tian, J.; Li, X. Research of Deformation and Soil Moisture in Loess Landslide Simultaneous Retrieved with Ground-Based GNSS. *Remote Sens.* **2022**, *14*, 5687. [CrossRef]
20. Davydzenka, T.; Tahmasebi, P.; Shokri, N. Unveiling the global extent of land subsidence: The sinking crisis. *Geophys. Res. Lett.* **2024**, *51*, e2023GL104497. [CrossRef]
21. Hasan, M.F.; Smith, R.; Vajedian, S.; Pommerenke, R.; Majumdar, S. Global land subsidence mapping reveals widespread loss of aquifer storage capacity. *Nat. Commun.* **2023**, *14*, 6180. [CrossRef]
22. Confuorto, P.; Soldato, M.D.; Solari, L.; Festa, D.; Bianchini, S.; Raspini, F.; Casagli, N. Sentinel-1-based monitoring services at regional scale in Italy: State of the art and main findings. *Int. J. Appl. Earth Obs. Geoinf.* **2021**, *103*, 102448. [CrossRef]
23. Rosi, A.; Tofani, V.; Agostini, A.; Tanteri, L.; Tacconi Stefanelli, C.; Catani, F.; Casagli, N. Subsidence mapping at regional scale using persistent scatters interferometry (PSI): The case of Tuscany region (Italy). *Int. J. Appl. Earth Obs. Geoinf.* **2016**, *52*, 328–337. [CrossRef]
24. Ciampalini, A.; Solari, L.; Giannecchini, R.; Galanti, Y.; Moretti, S. Evaluation of subsidence induced by long-lasting buildings load using InSAR technique and geotechnical data: The case study of a Freight Terminal (Tuscany, Italy). *Int. J. Appl. Earth Obs. Geoinf.* **2019**, *82*, 101925. [CrossRef]
25. Pirotti, F.; Adedipe, O.; Leblon, B. Sentinel-1 Response to Canopy Moisture in Mediterranean Forests before and after Fire Events. *Remote Sens.* **2023**, *15*, 823. [CrossRef]
26. Turner, J.A. *The Drought Code Component of the Canadian Forest Fire Behaviour System*; Technical Report; Canadian Forestry Service Headquarters: Ottawa, ON, Canada, 1972.
27. Charpentier, A.; James, M.; Ali, H. Predicting Drought and Subsidence Risks in France. *Nat. Hazards Earth Syst. Sci.* **2022**, *22*, 2401–2417. [CrossRef]

28. Understanding Italy. Climate of Italy. Available online: https://www.understandingitaly.com/climate.html (accessed on 10 October 2024).
29. Tosi, L. Land Subsidence in Italy: From a Few Well-Known Case Studies in the Past to Several Almost Unknown Occurrences at Present. In *Proceedings of the Workshop for Land Subsidence Prevention*; Institute of Geosciences and Earth Resources—National Research Council: Rome, Italy, 2019; p. 23.
30. Crosetto, M.; Solari, L. Chapter 4—European Ground Motion Service. In *Satellite Interferometry Data Interpretation and Exploitation*; Crosetto, M., Solari, L., Eds.; Elsevier: Amsterdam, The Netherlands, 2023; pp. 63–87. [CrossRef]
31. Wan, Z.; Hook, S.; Hulley, G. MOD11A1 MODIS/Terra Land Surface Temperature/Emissivity Daily L3 Global 1km SIN Grid V061. 2015. Available online: https://lpdaac.usgs.gov/products/mod11a1v061/ (accessed on 1 February 2024).
32. Funk, C.; Peterson, P.; Landsfeld, M.; Pedreros, D.; Verdin, J.; Shukla, S.; Husak, G.; Rowland, J.; Harrison, L.; Hoell, A.; et al. The Climate Hazards Infrared Precipitation with Stations—A New Environmental Record for Monitoring Extremes. *Sci. Data* **2015**, *2*, 150066. [CrossRef] [PubMed]
33. CEMS. CEMS Fire Historical v1. 2024. Available online: https://www.copernicus.eu/en/access-data/copernicus-services-catalogue (accessed on 6 September 2024).
34. Beall, H.W. *Canadian Forest Fire Danger Rating System*; Information Report FF-X-8; Canadian Forestry Service: Ottawa, ON, Canada, 1947.
35. Van Wagner, C.; Pickett, T. *Equations and FORTRAN Program for the Canadian Forest Fire Weather Index System*; Technical Report; Canadian Forest Service: Ottawa, ON, Canada, 1985.
36. Mutiibwa, D.; Strachan, S.; Albright, T. Land Surface Temperature and Surface Air Temperature in Complex Terrain. *IEEE J. Sel. Top. Appl. Earth Obs. Remote Sens.* **2015**, *8*, 4762–4774. [CrossRef]
37. Benali, A.; Carvalho, A.C.; Nunes, J.P.; Carvalhais, N.; Santos, A. Estimating Air Surface Temperature in Portugal Using MODIS LST Data. *Remote Sens. Environ.* **2012**, *124*, 108–121. [CrossRef]
38. Pirotti, F.; Toffah, F.E. Temperature, precipitation and drought code at 1 km resolution over Italy from start of 2017 to end of 2022 (6 years). *Zenodo* **2024**. [CrossRef]
39. Di Giuseppe, F.; Vitolo, C.; Barnard, C.; Libertá, G.; Maciel, P.; San-Miguel-Ayanz, J.; Villaume, S.; Wetterhall, F. Global seasonal prediction of fire danger. *Sci. Data* **2024**, *11*, 128. [CrossRef]
40. Van Wagner, C.E. *Development and Structure of the Canadian Forest Fire Weather Index System*; Canadian Forest Service: Ottawa, ON, Canada, 1987.
41. Ferretti, A.; Passera, E.; Capes, R. *End-to-End Implementation and Operation of the European Ground Motion Service (EGMS): Product Description and Format Specification*; Technical Report EGMS-D3-PDF-SC1-2.0-007; European Environment Agency, Copernicus Land Monitoring Service: Copenhagen, Denmark, 2021.
42. Crosetto, M.; Monserrat, O.; Cuevas-González, M.; Devanthéry, N.; Luzi, G.; Crippa, B. Measuring Thermal Expansion Using X-Band Persistent Scatterer Interferometry. *ISPRS J. Photogramm. Remote Sens.* **2015**, *100*, 84–91. [CrossRef]
43. Abdollahipour, A.; Ahmadi, H.; Aminnejad, B. A review of downscaling methods of satellite-based precipitation estimates. *Earth Sci. Inform.* **2022**, *15*, 1–20. [CrossRef]
44. Lockart, N.; Kavetski, D.; Franks, S.W. On the role of soil moisture in daytime evolution of temperatures. *Hydrol. Process.* **2013**, *27*, 3896–3904, [CrossRef]
45. Cook, B.I.; Mankin, J.S.; Anchukaitis, K.J. Climate Change and Drought: From Past to Future. *Curr. Clim. Chang. Rep.* **2018**, *4*, 164–179. [CrossRef]
46. Ma, P.; Lin, H.; Lan, H.; Chen, F. Multi-dimensional SAR tomography for monitoring the deformation of newly built concrete buildings. *ISPRS J. Photogramm. Remote Sens.* **2015**, *106*, 118–128. [CrossRef]
47. Bao, L.; Xing, X.; Chen, L.; Yuan, Z.; Liu, B.; Xia, Q.; Peng, W. Time Series Deformation Monitoring over Large Infrastructures around Dongting Lake Using X-Band PSI with a Combined Thermal Expansion and Seasonal Model. *J. Sens.* **2021**, *2021*, 6664933. [CrossRef]
48. Dal Moro, G.; Zadro, M. Subsurface deformations induced by rainfall and atmospheric pressure: Tilt/strain measurements in the NE-Italy seismic area. *Earth Planet. Sci. Lett.* **1998**, *164*, 193–203. [CrossRef]
49. Tanaka, T.; Shimojima, E.; Mitamura, K.; Hoso, Y.; Ishihara, Y. Precipitation, groundwater and ground deformation. In Proceedings of the Global and Regional Geodynamics: Symposium No. 101, Edinburgh, Scotland, 3–5 August 1989; Springer: New York, NY, USA, 1990; pp. 132–139.
50. Pavlyk, V.; Kutnyi, A.; Kalnyk, O. Features of the influence of seasonal variation of soil moisture on vertical movements of the earth's surface. *Geodynamics* **2019**, *2*, 16–23. [CrossRef]
51. Mimeau, L.; Tramblay, Y.; Brocca, L.; Massari, C.; Camici, S.; Finaud-Guyot, P. Modeling the response of soil moisture to climate variability in the Mediterranean region. *Hydrol. Earth Syst. Sci.* **2021**, *25*, 653–669. [CrossRef]
52. Qin, X.; Zhang, L.; Yang, M.; Luo, H.; Liao, M.; Ding, X. Mapping surface deformation and thermal dilation of arch bridges by structure-driven multi-temporal DInSAR analysis. *Remote Sens. Environ.* **2018**, *216*, 71–90. [CrossRef]